Article:
McCutcheon, J orcid.org/0000-0002-9114-7408, Power, IM, Shuster, J et al. (3 more authors) (2019) Carbon Sequestration in Biogenic Magnesite and Other Magnesium Carbonate Minerals. Environmental Science and Technology, 53 (6). pp. 3225-3237. ISSN 0013-936X

https://doi.org/10.1021/acs.est.8b07055

Carbon sequestration in biogenic magnesite and other magnesium carbonate minerals

Journal:	*Environmental Science & Technology*
Manuscript ID	es-2018-070555.R2
Manuscript Type:	Article
Date Submitted by the Author:	n/a
Complete List of Authors:	McCutcheon, Jenine; University of Leeds, School of Earth and Environment; Western University, Department of Earth Sciences Power, Ian; Trent University, Trent School of the Environment; The University of British Columbia, Department of Earth, Ocean and Atmospheric Sciences Shuster, Jeremiah; University of Adelaide, School of Biological Sciences; CSIRO Land and Water Harrison, Anna; Queen's University; Queen's University Dipple, Gregory; University of British Columbia, Department of Earth, Ocean and Atmospheric Sciences Southam, Gordon; The University of Queensland, School of Earth and Environmental Sciences

Carbon sequestration in biogenic magnesite and other magnesium carbonate minerals

Jenine McCutcheon[1,2], Ian M. Power[3,4], Jeremiah Shuster[5,6], Anna L. Harrison[7,8], Gregory M. Dipple[3], Gordon Southam[9]*

[1]Department of Earth Sciences, Western University, London, Ontario, N6A 5B7, Canada

[2]School of Earth and Environment, University of Leeds, Leeds, LS2 9JT, United Kingdom

[3]Department of Earth, Ocean and Atmospheric Sciences, The University of British Columbia, Vancouver, British Columbia, V6T 1Z4, Canada

[4]School of the Environment, Trent University, Peterborough, Ontario, K9L 0G2, Canada

[5]School of Biological Sciences, University of Adelaide, Adelaide, South Australia 5005, Australia

[6]CSIRO Land and Water, Glen Osmond, South Australia 5064, Australia

[7]Department of Geological Sciences and Geological Engineering, Queen's University, Kingston, Ontario, K7L 3N6, Canada

[8]School of Environmental Studies, Queen's University, Kingston, Ontario, K7L 3N6, Canada

[9]School of Earth & Environmental Sciences, The University of Queensland, St Lucia, Queensland 4072, Australia

*Corresponding contributor: j.mccutcheon@leeds.ac.uk

Keywords: carbon dioxide, cyanobacteria, magnesite, hydromagnesite, carbon sequestration, tailings, microbial carbonation, carbon pricing

Abstract

The stability and longevity of carbonate minerals make them an ideal sink for surplus atmospheric carbon dioxide. Biogenic magnesium carbonate mineral precipitation from the magnesium-rich tailings generated by many mining operations could offset net mining greenhouse gas emissions, while simultaneously giving value to mine waste products. In this investigation, cyanobacteria in a wetland bioreactor enabled the precipitation of magnesite ($MgCO_3$), hydromagnesite [$Mg_5(CO_3)_4(OH)_2 \cdot 4H_2O$], and dypingite [$Mg_5(CO_3)_4(OH)_2 \cdot 5H_2O$] from a synthetic wastewater comparable in chemistry to what is produced by acid leaching of ultramafic mine tailings. These precipitates occurred as micrometer-scale mineral grains and microcrystalline carbonate coatings that entombed filamentous cyanobacteria. This provides the first laboratory demonstration of low temperature, biogenic magnesite precipitation for carbon sequestration purposes. These findings demonstrate the importance of extracellular polymeric substances in microbially enabled carbonate mineral nucleation. Fluid composition was monitored to determine carbon sequestration rates. The results demonstrate that up to 238 t of CO_2 could be stored per hectare of wetland/year if this method of carbon dioxide sequestration was implemented at an ultramafic mine tailing storage facility. The abundance of tailings available for carbonation and the anticipated global implementation of carbon pricing make this method of mineral carbonation worth further investigation.

1. Introduction

Microbially-mediated carbonate mineral precipitation reactions, commonly referred to as microbial carbonation, have been documented in numerous environments, induced by organisms including cyanobacteria (*1-3*), sulfate reducing bacteria (*4, 5*), ureolytic bacteria (*6, 7*), and oxalotrophic bacteria (*8, 9*). This biogeochemical process has potential to produce stable, long-term sinks for atmospheric carbon dioxide (CO_2) (*10-13*). Stable carbonate minerals are a desirable sink for atmospheric CO_2, prompting the investigation of a range of carbon sequestration strategies that aim to precipitate carbonate minerals (*10, 11, 14-24*).

Passive carbonate mineral formation from ultramafic tailings produced by nickel, diamond, and asbestos mining operations has been studied at active and historic mine sites (*15, 25-28*). The high surface area of tailing minerals allows for greater weathering and carbonation reaction rates than those typically observed for natural bedrock (*29*). The ability of cyanobacteria to mediate the precipitation of hydrated magnesium carbonate minerals has been previously documented (*30-32*), and could be stimulated by utilizing soluble magnesium derived from dissolution of ultramafic tailings (*13, 33*). Cyanobacterial photosynthesis produces hydroxyl (OH^-) anions that promote carbonate mineral precipitation by increasing the pH value and thus the proportion of dissolved carbonate (CO_3^{2-}) species, as outlined in Reactions 1-3 (*34*). The extracellular surfaces of bacteria and their encapsulating exopolymer are negatively charged due to the presence of functional groups, such as carboxyls (*35*). These functional groups can bind divalent cations, thereby generating microenvironments with high cation concentrations that favor carbonate mineral precipitation reactions.

$$HCO_3^- + H_2O \rightarrow CH_2O + O_2 + OH^- \quad (1)$$

$$HCO_3^- + OH^- \rightarrow CO_3^{2-} + H_2O \quad (2)$$

$$5\ Mg^{2+} + 4\ CO_3^{2-} + 2\ OH^- + 4\ H_2O \rightarrow Mg_5(CO_3)_4(OH)_2 \cdot 5H_2O_{(s)} \quad (3)$$

Dypingite

The present study characterizes the ability of a phototrophic microbial consortium to drive Mg-carbonate mineral formation using atmospheric CO_2 in a wetland bioreactor (Figure 1). The bioreactor was inoculated with microbial mats predominantly composed of filamentous cyanobacteria that were collected from a natural wetland associated with a hydromagnesite-magnesite playa near Atlin, British Columbia, Canada (*32, 36, 37*). In addition to cyanobacteria, the microbial mats host abundant diatoms that remove dissolved silica from solution. The mats overlie anoxic sediments known to host sulfate reducing bacteria that have been previously shown to precipitate iron sulfide minerals (*37*). An Mg-rich synthetic mine wastewater, the chemistry of which was based on a tailings leaching experiment completed by McCutcheon et al. (*33*), was added to the bioreactor. Spatial and temporal changes in water chemistry and mineral precipitates were used to calculate the rate of carbon storage, thereby demonstrating this carbon sequestration strategy on a scale at least one order of magnitude greater than typical laboratory experiments.

2. Methods

2.1 Bioreactor design

In this 67-day experiment, synthetic mine wastewater and nutrient solutions were added to a 10 m long flow-through bioreactor constructed of 15 cm diameter polyvinyl chloride pipe (see Supplementary Information (SI) for details). The bioreactor was initially constructed for the experiment presented in McCutcheon et al. (*13*), in which the natural biogeochemical conditions of the wetland associated with the hydromagnesite-magnesite playa near Atlin were modelled. Prior to the present study, the microbial mats in the bioreactor were culled to allow for growth of

second generation mats containing no Mg-carbonate minerals (confirmed using electron microscopy). Rather than modelling the natural wetland, the present study targeted the biogeochemical conditions of an engineered mine site bioreactor wetland for the purposes of maximizing carbon sequestration in Mg-carbonate minerals. A critical experimental parameter by which the present study differs from its precursor is that an inorganic carbon source was not provided, which is crucial as the ingress of CO_2 into mineral carbonation reactors is a known limiting factor (*38*), and must be overcome for large-scale implementation of mineral carbonation. Additionally, the synthetic mine wastewater added to the bioreactor contained 5000 ppm (205.8 mM) Mg^{2+}. This value, which is five times greater than that used in the 2014 study, was based on the results of a tailings leaching experiment (*33*) in order to better represent an industrial tailing leachate. With dypingite as the target mineral (Reaction 3), the number of cycles of carbon fixation (Reaction 1) required to make the necessary hydroxyl and carbonate anions (Reaction 3) per molecule of dypingite produced was calculated as ten (*13*). The classic phytoplankton biomass formula $[(CH_2O)_{106}(NH_4)_{16}(H_3PO_4)]$ was used as a guideline to determine the phosphorous and nitrogen required in the nutrient solution (*39*). The synthetic mine wastewater solution chemistry was used to calculate the nutrient requirements of the microbes in the bioreactor using modified BG-11 growth medium (SI Tables S1 and S2) (*40*). The solutions were added to one end of the bioreactor (0 m), from which they could passively flow through the gravity-driven system and drain out the other end. A second nutrient solution inflow was located at 5 m. The inflow rate of both solutions was increased over time to determine the response of the bioreactor to a high influx of soluble magnesium (Table 1). The bioreactor was housed in greenhouse with an average air temperature of 23.5°C, as documented at all sampling time points, and subject to diurnal 12 h

light/dark conditions. The experiment took place in southern Canada from December to March, and thus the light was provided by a combination of natural and artificial sources.

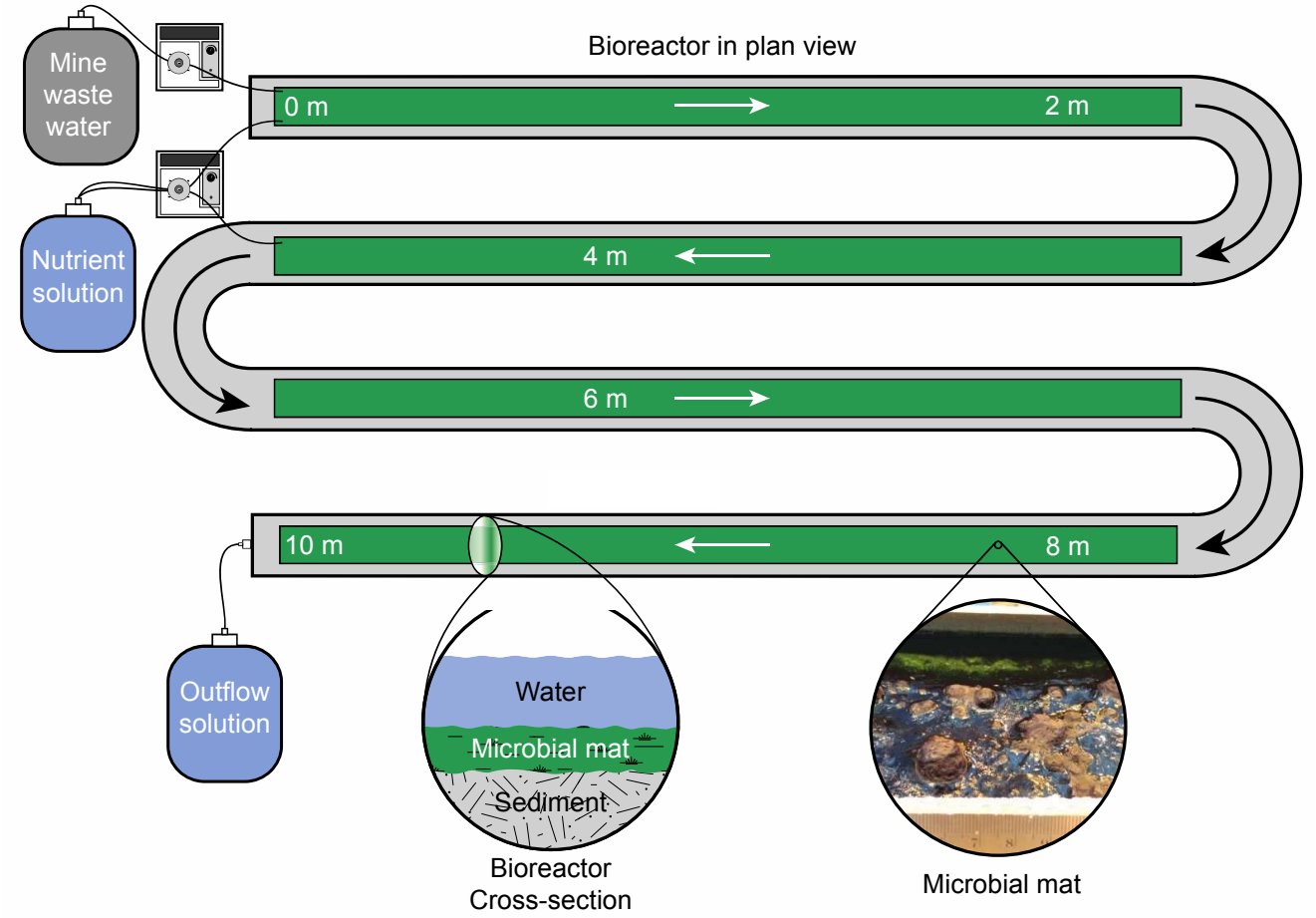

Figure 1. Plan view schematic of the bioreactor inoculated with microbial mats for the carbonation experiment. The synthetic mine wastewater was added at one end of the channel (0 m), while the nutrient solution was added at 0 m and 5 m. The gravity driven system allowed for the solution to flow passively through the bioreactor and out a valve in the other end. Arrows indicate the direction of flow. The four straight segments of the bioreactor were open to the air and contained the active microbial mats (green segments in the schematic), while the bends were covered. A cross-section of the bioreactor contents is shown, along with a photograph of the pellicle that formed at the air-water interface.

After 21 days, a pellicle, a biofilm at the air-water interface, developed as sections of mat were buoyed up to the water surface by trapped photosynthetically-generated oxygen bubbles. The pellicle was removed because it was restricting the photosynthesis of the benthic microbial mats and causing a decrease in dissolved oxygen concentration in the bioreactor water. At this time, the

addition of the wastewater solution was ceased and the growth medium concentration was halved to moderate microbial activity (Table 1). The bioreactor outflow volume was measured to quantify evaporation, which indicated that 45% of the added water evaporated during the experiment. This water loss was taken into account for mass balance calculations for the system and when interpreting conductivity, inductively coupled plasma-atomic emission spectroscopy (ICP-AES), ion chromatography (IC), and dissolved inorganic carbon (DIC) results (SI Table S3).

Table 1. Fluid composition for the nutrient and synthetic mine wastewater solutions added to the bioreactor during the carbonation experiment. Summary of the timeline for solution addition to the bioreactor at the 0 and 5 m locations. Note, the experiment was paused between day 21 and 32 due to the formation of the pellicle.

	Fluid composition measurements			Cation and anion concentrations (mM)					
Solution type	**pH**	**DO (mg/mL)**	**Conductivity (mS/cm)**	**Mg^{2+}**	**Ca^{2+}**	**DIC**	**PO_4^{3-}**	**NO_3^-**	**NO_2^-**
100% nutrient solution	5.91	4.20	6.64	0.01	0.78	0.20	6.10	74.9	0.00
50% nutrient solution	5.91	6.11	3.65	0.00	0.34	0.20	2.28	30.7	0.00
Wastewater	8.10	7.37	18.1	196	8.16	0.21	0.00	0.00	0.00

Solution addition timeline				
	0 m solution addition point		5 m solution addition point	
Day	**Solution**	**Flow rate (L/day)**	**Solution**	**Flow rate (L/day)**
1-21	100% nutrients	1	100% nutrients	1
	Wastewater	1		
21	Experiment paused and the pellicle removed			
22-31	Standard BG-11	1	Standard BG-11	1
32	Experiment resumed			
32-38	50% nutrients	1	100% nutrients	1
	Wastewater	1		
39-45	50% nutrients	2	50% nutrients	2
	Wastewater	2		
46-52	100% nutrients	3		
	Wastewater	3		
53-59	100% nutrients	4		
	Wastewater	4		
60-67	50% nutrients	5		
	Wastewater	5		

2.2 Mineral and microbe characterization

Microbial mat samples collected at 0 m prior to the experiment, and at 0 m, 5 m, and 10 m on days 28 and 67 were analyzed using X-ray diffraction (XRD). The mats were air dried in petri dishes and powdered using a mortar and pestle. The samples were analyzed using a Bruker D8

Focus Bragg-Brentano diffractometer and mineral phases were determined using DIFFRAC^{plus} Eva software (see SI for details). Additional microbial mat samples were collected on days 14 and 28 from the same locations representing upstream, midstream, and downstream mats for analysis using scanning electron microscopy and energy dispersive spectroscopy (SEM-EDS; see SI for details). After 67 days, microbial mats were sampled at 1 m increments for SEM-EDS. A sample of microbial mat collected from the 10 m location in the bioreactor on day 67 was fixed using $2\%_{(aq)}$ glutaraldehyde, and stained using $2\%_{(aq)}$ OsO_4, $1.5\%_{(aq)}$ ferricyanide, and $1\%_{(aq)}$ thiocarbohydrazide prior to being dehydrated using acetone, and embedded in Epon Embed 812 resin, described in detail in McCutcheon and Southam (*41*) as a protocol adapted for use on natural microbial biofilms (*42*). Ultrathin sections of the embedded sample were characterized using transmission electron microscopy (TEM) in conjunction with selected area electron diffraction (SAED) and EDS (see SI for details).

2.3 Fluid composition analyses

Fluid composition was monitored weekly at 1 m increments along the length of the bioreactor. Dissolved oxygen (DO), pH, and conductivity were measured using probes (see SI for details). Water samples were collected and filtered (0.1 μm pore-size) to determine DIC, and major cation (ICP-AES) and anion (IC) concentrations at each location (see SI for details). Due to the high concentration, magnesium was analysed using IC instead of ICP-AES. Stable carbon isotopic measurements of DIC is another means of determining whether a solution is at equilibrium with atmospheric CO_2 (*25*). Stable carbon, oxygen, and hydrogen isotope analysis was conducted on water samples collected 1 week after the experiment concluded (see SI for details). Saturation indices (*SI*) for possible mineral products were determined using PHREEQC (*43*) and the fluid

composition data were used to evaluate how pH, and the availability of Mg^{2+} and DIC species influence carbonate mineralization (see SI for PHREEQC details).

3. Results

3.1 Carbonate mineral precipitation

XRD analysis of the pre-experiment microbial mat sample identified thenardite (Na_2SO_4) and aragonite ($CaCO_3$) (SI Figure S1A), neither of which were observed with SEM (SI Figure S2A). Magnesite, hydromagnesite, dypingite, aragonite ($CaCO_3$), and nesquehonite [$Mg(HCO_3)(OH)\cdot 2H_2O$] were identified as mineral precipitates in the bioreactor microbial mats using XRD (Figure 2, SI Figure S1B,C). Subhedral rhombohedral magnesite crystals were predominantly observed between 4 and 10 m in the bioreactor and were identified using TEM-EDS and SAED (Figure 3A,B, SI Table S4). The magnesite often occurred at convergent points between multiple hydromagnesite plates (Figure 3C-E), a relationship documented in natural samples by Power et al. (*36*). Note the tendency of magnesite crystals to fall out of the ultrathin sections, as seen in Figure 3E. For those that were retained, SAED confirms that these precipitates are hexagonal, and indicates that they are polycrystalline in nature (Figure 3A,B).

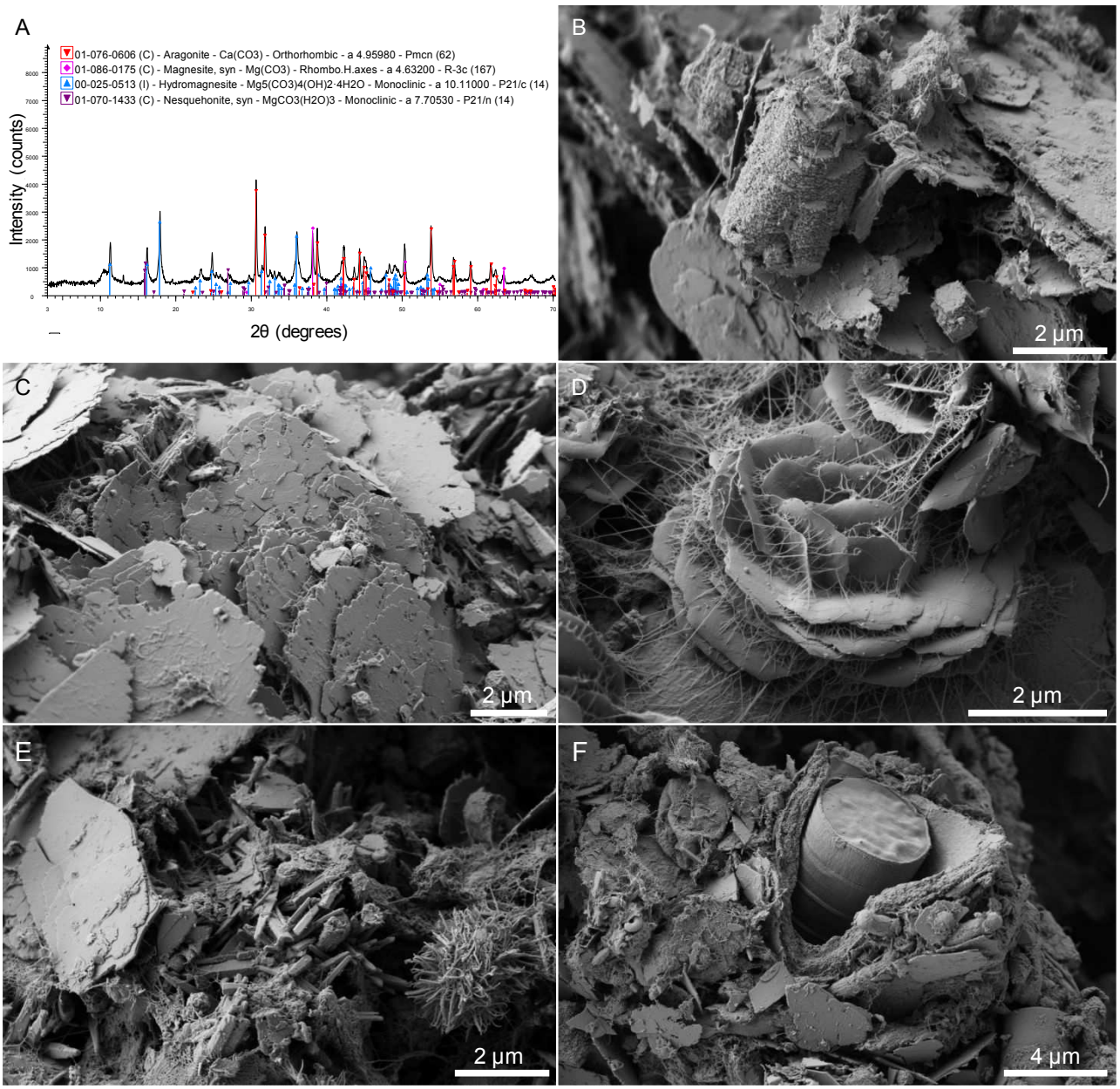

Figure 2. X-ray diffraction and SEM results for the key mineral precipitates produced in this study. A: Pattern produced by XRD analysis of a sample of microbial mat collected at 5 m on day 67 of the carbonate precipitation experiment. Scanning electron micrographs depicting: B: rhombohedral magnesite crystals found between 4 and 10 m in the bioreactor; C: platy hydromagnesite or dypingite crystals formed throughout the bioreactor; D: a rosette of hydromagnesite or dypingite covered in EPS (day 67, 1 m); E: platy hydromagnesite or dypingite crystal (left), disarticulated aragonite crystals (centre), and mineral coated coccoid bacterium (right); and F: cyanobacterium filament encased in Mg-carbonate encrusted EPS (day 14, 10 m).

Hydromagnesite or dypingite crystals were the most abundant precipitates and occurred as plates and rosettes, often associated with large amounts of extracellular polymeric substances (EPS; Figure 2C,D). The EPS exhibits the collapsed, mesh-like morphology commonly observed

when biofilms are prepared for SEM via solvent dehydration and critical point drying (*41*). The platy hydromagnesite or dypingite precipitates visible using SEM (Figure 4A) can also be observed using TEM, oriented tangential to the filamentous cells such that only the edge of the platy crystals can be observed (Figure 4B). The platy precipitates can be observed nucleating on EPS surrounding filamentous cyanobacteria (Figure 4B,C), as demonstrated by McCutcheon and Southam (*41*). In addition to crystalline precipitates, cells and surrounding EPS often appear coated in microcrystalline precipitates (Mg-C-O based on EDS), resulting in cells becoming entombed (Figure 2F), likely interfering with microbial metabolism. Many empty Mg-carbonate casts exhibiting the morphology of cyanobacterium filaments were observed using TEM (Figure 4D) and SEM (Figure 4E,F), appearing to encase a framework of EPS. Poorly crystallized ~100 nm-scale pseudo-acicular precipitates composed of Ca-Mg-C-O-P formed directly on coccoid microbial cells (Figure 2E, 4G,H), much like the extracellular precipitate morphology observed by Shuster et al. (*44*).

Aragonite was observed as prismatic crystals (SI Figure S2B,C), similar to those documented by Power et al. (*37*) from sediments in the Atlin wetland (See SI for aragonite and nesquehonite results). Struvite ($NH_4MgPO_4 \cdot 6H_2O$) was identified in the samples collected from the bioreactor, with this mineral phase being most abundant at 0 m and 5 m (SI Figure S2E,F).

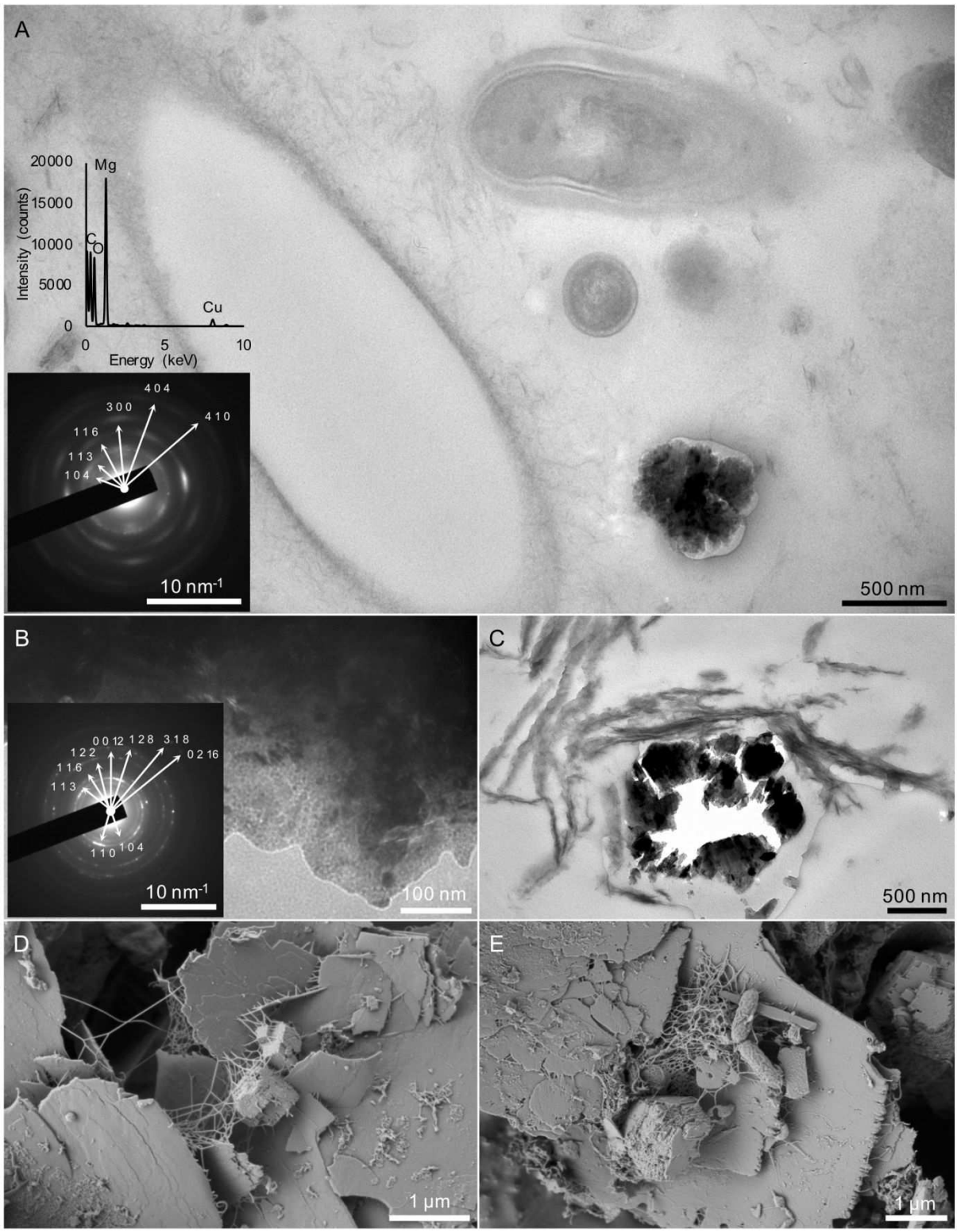

Figure 3. Transmission electron micrographs showing A: the microbial biofilm in ultrathin section, including a magnesite grain (corresponding SAED pattern and spectrum on left) adjacent to the EPS outline of a cell; B: a magnesite grain in ultrathin section with corresponding SAED (inlay); and C: a magnesite grain (centre) at the junction between platy hydromagnesite crystals. Note the tendency of magnesite to fall out of the ultrathin section (C). D and

E: Secondary electron micrographs depicting the same magnesite-hydromagnesite relationship visible in (C), over which a coating of EPS can be observed.

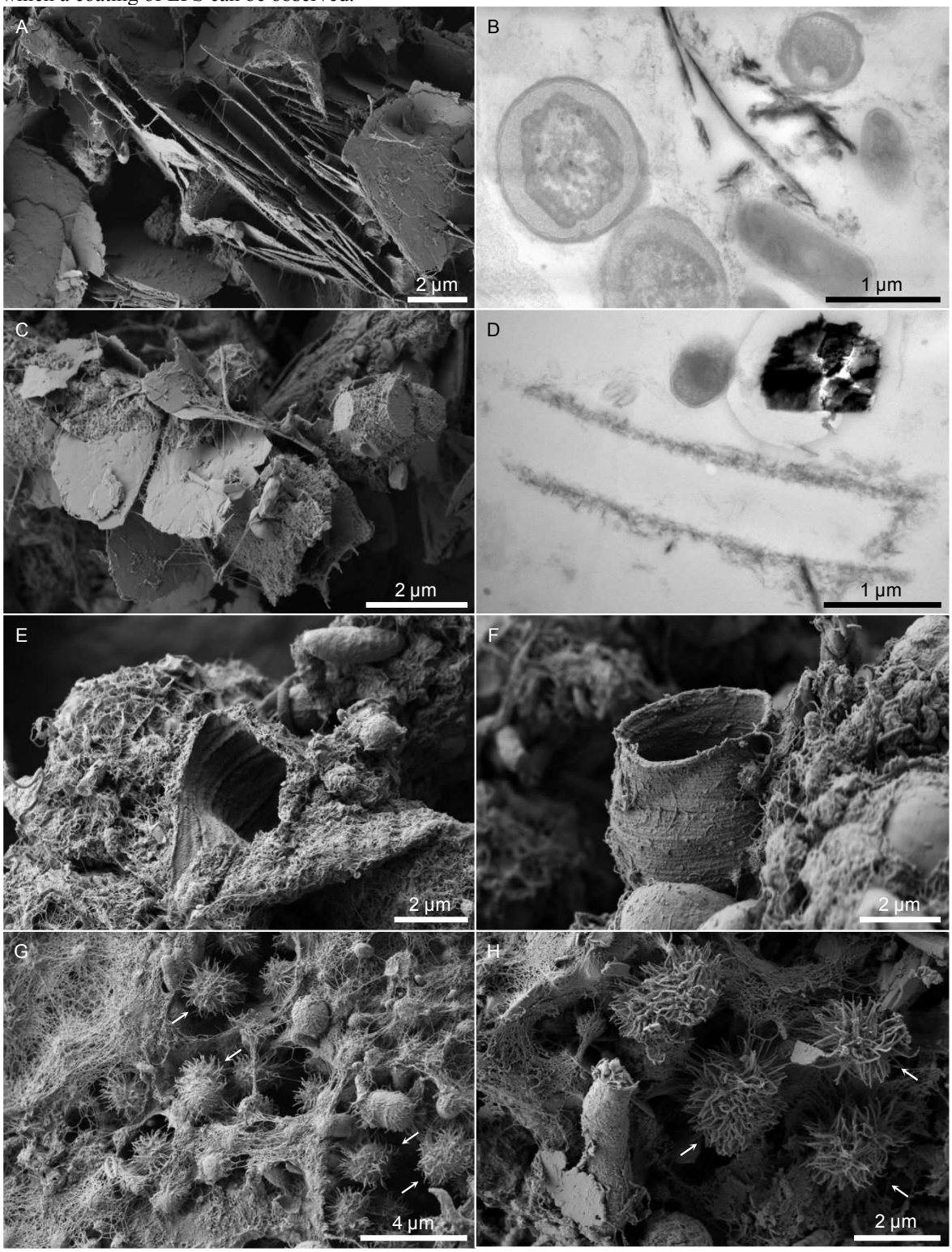

Figure 4. A: Secondary electron micrograph showing the platy hydromagnesite crystals. B: Transmission electron micrograph showing platy hydromagnesite crystals as they nucleate on EPS adjacent to filamentous cyanobacteria (visible here in cross-section). EPS-nucleated hydromagnesite and mineral encrusted EPS outlining cyanobacterium filaments visible using C: SEM and D: TEM. Note the magnesite crystal visible in the top right corner of both C and

D. E and F: Casts of filamentous bacteria composed of magnesium carbonate. Scanning electron micrographs of G: the large amount of EPS generated in the bioreactor along with the microcrystalline pseudo-acicular mineral precipitate (H) found coating coccoid cells within the microbial mat (coated cells indicated by arrows in G and H).

3.2 Fluid composition

The pH and DO concentrations both decreased during the first 21 days of the experiment, coincident with the formation of the pellicle, from respective system averages of 9.8 and 15.2 mg/L on day 0, to 9.4 and 5.9 mg/L on day 21 (Figure 5A,B; SI Table S5). The conductivity, and Mg^{2+} and Ca^{2+} concentrations increased over time with the increase in flow rate from day 39 to 67, while spatially, these three parameters decreased down the length of the bioreactor (Figure 5C-E). With a wastewater inflow rate of 1 - 3 L/day, the bioreactor precipitated carbonate minerals at a rate that reduced the conductivity and magnesium concentration to equal or less than the Time = 0 values (Figure 5C-E). Conductivity (Figure 5C) and magnesium concentration (Figure 5D) values increased with inflow rates of 4 and 5 L/day despite magnesium continuously being removed from the water, suggesting the influx exceeded the rate of removal via precipitation. The average magnesium concentration of the entire bioreactor increased from 2.6 mM to 68.8 mM over time, owing to the increased inflow rate (Figure 5D, SI Table S5).

The DIC was relatively constant during the first 21 days, after which it decreased as the wastewater inflow rate was increased (Figure 5F; SI Table S5). DIC concentrations increased with distance from the source of nutrient and synthetic mine wastewater input at 0 m and 5 m. Higher nutrient availability at these locations may have caused localized increases in heterotrophy; however, it appears that autotrophy dominated the microbial activity beyond 5 m, resulting in a pH value increase due to photosynthesis driven CO_2 consumption and OH^- generation. The DIC concentration on day 67 was 64% of what was measured on day 60, indicating rapid removal of

DIC from solution via carbonate precipitation (SI Table S5). Note, approximately 11% of this decrease is due to the increase in flow rate.

The phosphate concentration showed no clear trend during the first 21 days of the experiment, apart from a clear increase in concentration at the 5 m sampling location, corresponding to the second nutrient addition point (Figure 5G; SI Table S5). From day 39 to 67, the phosphate concentration approached 0, and never increased above 0.1 mM. The nitrate concentration was irregular during the first 21 days, after which nitrate accumulated over time to a system average concentration of 17.3 mM on day 67 (Figure 5H). The nitrate concentration decreased down the length of the bioreactor. No nitrite was measured in the nutrient solution or mine wastewater (Table 1). The nitrite concentration was irregular in the bioreactor during the first 21 days, fluctuating between 0.04 and 1.15 mM (Figure 5I). From day 39 to 67, the nitrite concentration decreased markedly to less than 0.1 mM (Figure 5I; SI Table S5).

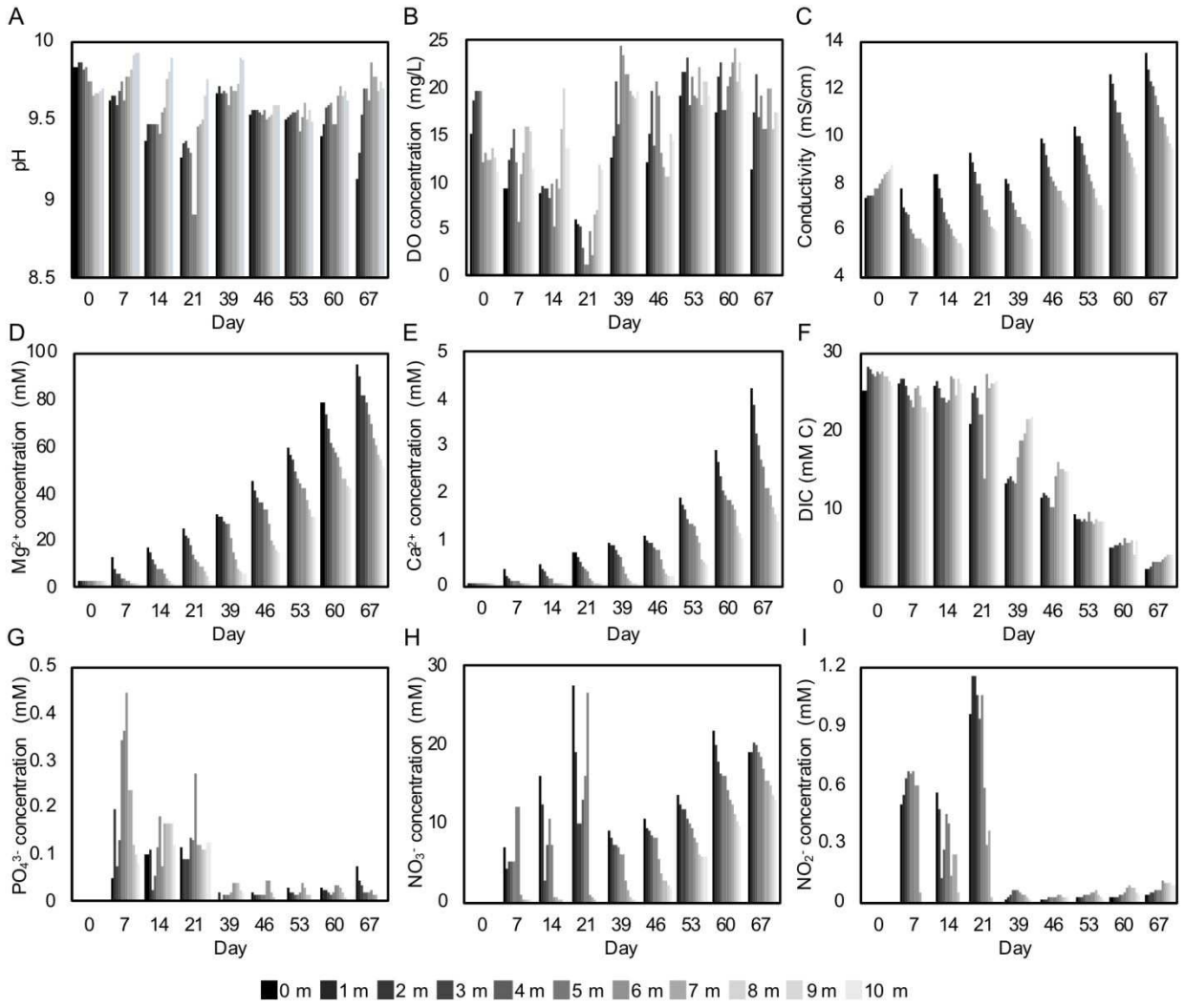

Figure 5. Change in the fluid composition parameters down the length of the bioreactor over the duration of the experiment. A) pH, B) dissolved oxygen, C) conductivity, D) Mg^{2+}, E) Ca^{2+}, F) DIC, G) phosphate, H) nitrate, and I) nitrite. Note, no phosphate, nitrate, or nitrite data is available for day 0.

On day 67, the δ^2H and $\delta^{18}O$ values of the water increased with distance down the bioreactor length (Table 2). The equilibrium fractionation between $CO_{2(g)}$ and HCO_3^-, the dominant DIC species at the experimental pH, is +7.9‰ at 25°C (*45*), and the $\delta^{13}C$ value of atmospheric CO_2 is approximately -8.3‰ (*46*). The stable carbon isotope analysis indicated that the $\delta^{13}C_{DIC}$ was -6.76‰ at 0 m and decreased down the length of the bioreactor to -9.04‰ at 10

m (Table 2), while the DIC concentration increased from 2.42 to 4.16 mM over the same distance (SI Table S5).

Table 2. Stable isotope data for water samples collected following the carbonate precipitation experiment.

Sample location	$\delta^{13}C$ (‰)	$\delta^{2}H$ (‰)	$\delta^{18}O$ (‰)
0 m	-6.76	-27.3	-0.32
1 m	-7.17	-31.12	0.08
2 m	-7.99	-28.93	0.12
3 m	-9.15	-23.38	0.27
4 m	-8.97	-27.3	0.47
5 m	-9.35	-23.3	0.24
6 m	-8.99	-26.57	1.25
7 m	-8.59	-27.28	1.43
8 m	-8.77	-23.7	2.09
9 m	-8.92	-20.62	2.64
10 m	-9.04	-14.9	2.43

Carbonate mineral Saturation Indices (*SI*) were calculated using the fluid composition data and PHREEQC (SI Tables S6-24). The synthetic mine wastewater had *SI*s for hydromagnesite and magnesite of -10.07 and -0.65, respectively. On day 0, the sampling locations in the bioreactor had hydromagnesite and magnesite *SI*s ranging between -0.36 and 0.51, and 1.39 and 1.45, respectively. The average hydromagnesite *SI* for the bioreactor increased from 0.05 (day 0) to 3.64 (day 39) followed by a decrease over the remainder of the experiment. The system average *SI* for magnesite increased over time from 1.43 on day 0 to 2.09 on day 39, followed by a decrease to 1.62 by day 67 (SI Table S23). The average magnesite *SI* by sampling location changed little over time, remaining between 1.72 and 1.86. On the final day of the experiment (day 67), the magnesite *SI* increased down the length of the bioreactor from 1.2 (0 m) to 1.81 (10 m). The bioreactor did not reach equilibrium with atmospheric $pCO_{2(g)}$ at any point during the experiment (SI Table S19). The calculated pCO_2 in equilibrium with the measured DIC values was in the range of 1.0 to 158 ppm (SI Table S19).

4. Discussion

4.1 Microbial magnesium carbonate mineral precipitation

The trends observed between Mg-carbonate type and location in the bioreactor can be explained using Ca-carbonate precipitation kinetics (*47-50*), as carbonate crystal size and abundance is dependent on the balance between crystal nucleation rate and crystal growth rate. Higher degrees of supersaturation promote mineral nucleation, resulting in a greater abundance of individual crystals (*48, 50*), a relationship observed in the upper 5 m of the bioreactor as rapid nucleation of the microcrystalline coatings on microbial cells. In contrast, crystal growth is favored over crystal nucleation in solutions with a low degree of supersaturation and results in fewer, larger crystals. This relationship is evident in the downstream 5 m of the bioreactor, where micrometer-scale hydromagnesite and magnesite grains were the prevailing precipitates.

Microbial mats aid carbonate mineral nucleation, in part, by assisting the dehydration of divalent cations. This is a particularly critical precursor in the case of Mg-carbonates, which are more difficult to precipitate than their calcium counterparts. Mg^{2+} ions in solution are enclosed in a stable hydration shell composed of two layers of water molecules (*51, 52*). The inner layer consists of an octahedrally coordinated shell of six water molecules, around which a second shell of twelve water molecules is bound by hydrogen-bonds (*52-54*). The hydration energy of magnesium (1926 kJ/mol) compared to calcium (1579 kJ/mol) results in water molecule exchange in calcium's hydration shell occurring ~1000× faster than around magnesium (*55, 56*), resulting in much lower precipitation rates of anhydrous Mg-carbonates compared to Ca-carbonates, and thus the tendency to form hydrated Mg-carbonates at low temperature. The biogenic process by which the magnesite identified using TEM-SAED-EDS formed explains why the lattice spacings for

these precipitates do not precisely match reference values (*57*) (Figure 3, SI Table S4). Biogenic carbonate minerals tend to exhibit a higher degree of crystal lattice disorder than their abiotically synthesized counterparts (*58, 59*), a characteristic that is detectable using SAED (*60*).

Abiotic precipitation of magnesite at temperatures below 80°C is typically inhibited by the energy required for the spiral step crystal growth pattern by which magnesite forms (*61*). However, Power et al. (*51*) demonstrated that the hydration shell surrounding Mg^{2+} ions can be disrupted by binding to carboxyl-coated polystyrene microspheres, thereby inducing low temperature magnesite precipitation. The results of the present study demonstrate that the negatively charged cell exteriors and EPS in cyanobacterial mats are capable of facilitating Mg^{2+} dehydration through a similar mechanism (*32*). As much as 90% of the total organic carbon in biofilms is found in the EPS, which comprises a matrix of water, polysaccharides, lipids, proteins, and nucleic acids (*62*). Extracellular polysaccharides provide a large proportion of the stability of biofilms (*63*), which is influenced by the prevalence of cation binding. Cross-linking of polysaccharides in the EPS with cations can increase biofilm stability, while simultaneously generating localized microenvironments of high cation concentrations (*64*). The EPS becomes a cation reservoir to which low molecular weight (LMW) organic compounds can attach. Heterotrophic metabolic processes oxidize these LMW compounds to product bicarbonate, which can subsequently react with the cations to form carbonate minerals (*64*). Mineral precipitates may remain attached to the EPS, as in the case of the cellular carbonate coatings (Figure 4C), or be released like many of the hydromagnesite plates observed using SEM (Figure 4A). The apparent tendency for hydromagnesite to nucleate on, and subsequently be shed from, EPS was demonstrated by McCutcheon and Southam (*41*), and highlights that microbial mats must be actively producing and metabolizing EPS to provide carbonate mineral nucleation sites.

Carbonate precipitation can lead to mat lithification, a process demonstrated in the rock record and many contemporary environments (*4, 65-67*). For the reasons outlined above, calcium, rather than magnesium, carbonate minerals are the predominant deposits found in natural settings and throughout the rock record. The formation of magnesite, versus less stable, hydrated Mg-carbonate mineral phases is likely dependant on the optimization of a number of factors, namely: the efficiency of the biogeochemical process of cation dehydration described above, development of EPS-hosted microenvironments of high Mg^{2+} concentration, and alkalinity generation via microbial metabolism. Hydrated Mg-carbonate minerals, such as hydromagnesite, typically dominate known Mg-carbonate deposits because the magnesium ions need not be completely dehydrated (*61, 68*), thus making the successful demonstration of low temperature, microbially-aided magnesite precipitation in the present study noteworthy.

4.2 Microbial activity and fluid composition

Some of the CO_2 used in carbonate precipitation may have been generated by heterotrophic oxidation of photosynthetically-derived organic compounds, and contributed to DIC by producing dissolved CO_2 or HCO_3^- (*12, 69*). Organic matter in microbial mat systems is largely derived from atmospheric carbon fixed by phototrophs, which can be oxidized by heterotrophs, providing an indirect pathway for transferring atmospheric CO_2 into water (*12*). Heterotrophic activity, therefore, may have been partially responsible for the patterns observed in the DIC, a possibility supported by the depletion in $^{13}C_{DIC}$ (*70*). Phototrophic metabolism preferentially removes $^{12}C_{DIC}$ thereby enriching the remaining DIC pool in ^{13}C while decreasing DIC concentrations (*71*). Carbonate precipitation may decrease both DIC concentration and $\delta^{13}C_{DIC}$ values (*25*). However, for the majority of the bioreactor length, $\delta^{13}C_{DIC}$ values and DIC generally co-vary, likely due to dissolution of atmospheric CO_2, as this will increase both DIC and $\delta^{13}C$ values. Progressive

increases in $\delta^{2}H$ and $\delta^{18}O$ from -27.3‰ and -0.3‰ to -14.9‰ and 2.4‰, respectively, can be attributed to evaporation along the length of the bioreactor (Table 2) (*72*).

Saturation indices cannot be used as strict indicators of Mg-carbonate precipitation, given kinetic limitations to precipitation; however, the following interpretations regarding the relationship between fluid composition, *SI*, and mineral precipitation can be made (*13*). The changes in magnesium concentration indicated that the greatest carbonation rate was achieved from day 60 - 67 and carbonate precipitation was pervasive throughout the bioreactor. The low hydromagnesite *SI* values calculated for day 67 are consistent with rapid mineral precipitation and may be responsible for the observed cyanobacteria entombment. The pH and DO measurements from days 60 and 67 suggest that this mineralization caused a decline in photosynthesis, with the system average pH value decreasing from 9.59 to 6.21, and system average DO from 21.0 mg/L to 17.4 mg/L (SI Table S5). Addition of 5000 ppm magnesium at a rate of 5 L/day was likely approaching the limit of the bioreactor's ability to consume magnesium; therefore, reducing the flow rate or the magnesium concentration would be necessary for long-term maintenance of the biogeochemical conditions required for carbonation.

The pellicle likely limited gas exchange between the atmosphere and bioreactor water, as well as photosynthesis in the submerged microbial mats. Reduced photosynthesis plus heterotrophic consumption of oxygen resulted in a suboxic environment that potentially stimulated sulfate reducing-bacteria (SRB) activity, organisms previously found in the anoxic sediments used to line the bottom of the bioreactor (*37*). These organisms use sulfate (SO_4^{2-}) as a terminal electron acceptor to oxidize organic compounds, producing hydrogen sulfide (H_2S) (*73, 74*), which can consume oxygen, support anoxygenic photosynthesis, and/or be toxic to cyanobacteria (*75-77*). The metabolic activity of SRBs would have increased as DO decreased, especially at night (*75*).

While SRBs can enable carbonate precipitation by driving the water chemistry conditions towards carbonate supersaturation and generating EPS (*4, 5*), the toxicity of H_2S towards cyanobacteria was likely detrimental to the overall bioreactor function (*78*). Thus, the pellicle formation demonstrates the need to regulate nutrient input, microbial growth, and carbonate precipitation, such that biofilm formation does not outpace the bioreactor's capabilities.

The elevated concentration of nitrite during the initial 21 days of the experiment (Figure 5I) is consistent with nitrate consumption by denitrifying bacteria in anaerobic biofilms (*79*), which would be enabled by the low DO conditions caused by the pellicle. Nitrite is part of active nitrogen fixation-nitrification-denitrification reaction pathway common in cyanobacteria-dominated microbial mats. The nitrite depletion that occurred following the removal of the pellicle and corresponding reoxygenation of the water suggests that anaerobic denitrification was the source of the nitrite (*80*). The disappearance of nitrite after day 21, corresponding to the loss of the pellicle and re-oxygenation of the bioreactor suggests that denitrification was the source of the nitrite.

4.3 Quantifying mineral precipitation rate and application to carbon sequestration

This study demonstrated that atmospheric CO_2 can be sequestered via microbial carbonation in an engineered system, which is important because dissolution of atmospheric CO_2 into water is typically the rate-limiting step in mineral carbonation experiments and in mine tailings (*14, 25*). The water chemistry data, flow rate, and microbial mat surface area were used to calculate mineral precipitation and carbon storage rates. Carbon storage in biomass is considered in addition to storage in mineral phases; as its presence was minimal, aragonite was excluded from the storage calculation. See SI for details regarding how struvite precipitation was accounted for in the biomass calculation.

379 The first week (day 0-7; inflow: 1 L/day) of the experiment exhibited the highest proportion
380 of magnesium removed (98%); however, the greatest mass of carbonate precipitated occurred
381 during the final week of the experiment (day 60-67; inflow: 5 L/day) with 73% of the added
382 magnesium being used for carbonate precipitation. During the final week, 5.05 mol or ~123 g of
383 Mg was used to produce carbonate minerals. A carbon sequestration rate can be calculated for each
384 of hydromagnesite and magnesite, providing a range for mineral carbonation. It was calculated
385 that 472 g of hydromagnesite or 426 g of magnesite could have formed in the bioreactor during
386 the final week. Extrapolating this process to the scale of a microbial carbonation wetland at a mine
387 tailings storage facility, these values translate to combined biomass and mineralogical carbon
388 storage rates of 222 and 238 t of CO_2/ha of wetland/year for hydromagnesite and magnesite,
389 respectively. The hydration of hydromagnesite results in a slightly greater precipitate mass when
390 compared to magnesite, but makes it slightly less efficient in terms of carbon stored per magnesium
391 atom.

392 The undersaturation of the bioreactor water with respect to atmospheric CO_2 suggests that
393 sequestration rates could be increased by providing additional carbon. Harrison et al. (*14*)
394 demonstrated that supplying gas containing 10% CO_2, similar to power plant flue gas, causes a
395 240-fold increase in the rate of Mg-carbonate mineral precipitation in brucite [$Mg(OH)_2$]-bearing
396 slurries. Limited availability of water in dry tailings can also inhibit hydrated magnesium
397 carbonate mineral precipitation (*81*). An in situ microbial mineral carbonation experiment by
398 McCutcheon et al. (*82*) demonstrated the challenge of water limitation, in which a microbial
399 inoculum, cultured from biofilms naturally occurring at the mine site, was added to chrysotile mine
400 tailings for the purpose of producing a Mg-carbonate crust. Those results indicated that
401 constructing microbial carbonation wetlands, similar to the one implemented in the present study,

is likely the best strategy for integrating microbial carbonation technology for industrial carbon sequestration at tailing storage facilities (*82*). A potential deployment strategy would include the production Mg-rich fluids via large-scale leaching of mafic or ultramafic mine tailings, which would act as a feedstock for carbonation wetlands that could be constructed in the open pits remaining from mining activity (*82*). Carbonate mineral precipitation in the wetlands could utilize atmospheric CO_2, while simultaneously sequestering first row transition metals that may be released from the tailings during acid leaching, thus reducing the risk of toxic metal contamination of the surrounding environment (*83, 84*). Similar to the wetland near Atlin, which hosts sulfate reducing bacteria in the underlaying anoxic sediments, any sulfate accumulating in the system could be consumed through iron sulphide mineral generation by SRBs (*37*).

Microbial mat lithification would occur as a more laterally extensive variation of the cementation observed in naturally occurring stromatolites, exhibiting progressive growth and cementation over time. The mats would grow upwards as lithification progresses, maintaining an active layer of microbial mat into which the ion-rich leach solution can infiltrate, thereby receiving the reactants required for carbonate precipitation. Through this process, the pit would gradually become infilled with the resulting precipitates, forming a carbonate deposit. The stability of the deposit should be monitored in order to ensure safe mine site reclamation.

As a measure of scale for the deployment of this carbon sequestration strategy, applying this technology to the Mount Keith Nickel Mine (Western Australia) would require a 1900 ha bioreactor, a size comparable to the existing tailings facility. Such a wetland could sequester 422 000 to 450 000 t of CO_2/year, which is ~10% of the estimated 4 Mt CO_2/year sequestration capacity of the Mount Keith tailings facility (*85*). The remaining capacity could be satisfied using other acceleration strategies, such as flue gas injection (*14*). In 2004, the Mount Keith Mine emitted

425 ~382 000 t of CO_2 equivalent, demonstrating that the proposed carbon storage strategy is capable
426 of sequestering mine-scale quantities of CO_2 (*12*). With the correct balance of nutrients, e.g., the
427 limiting phosphate concentrations encountered in this study (Fig. 5), microbial growth and mine
428 wastewater input, the carbonate precipitation rate could be increased. If successful, this technology
429 could fulfil a portion of the ~175 Mt CO_2/year total carbon sequestration capacity estimated for
430 the ~419 Mt of mafic and ultramafic tailings that are generated worldwide each year (*86, 87*).
431 The lack of a global carbon price is a fundamental limiting condition for the development
432 of mineral carbonation strategies beyond laboratory demonstrations for large-scale industrial
433 implementation (*86*), however, estimates by the High-Level Commission on Global Carbon Prices
434 indicate that meeting the temperature target of the Paris Agreement will necessitate carbon prices
435 of $50-100 USD/t CO_2 by 2030 (*88*). At a conservative price of $50 USD/t, economic valuation
436 of microbial carbonation of nickel mine tailings, considering past production and reserve ore at
437 major ultramafic nickel mine sites worldwide (excluding other ultramafic mine tailings), puts the
438 prospective worth of this microbial carbon storage technology at $20.5 billion USD (*89, 90*). Such
439 a valuation is encouraging, as it will be necessary for many countries to increase their carbon price
440 to achieve their emission reduction targets (*88*). For instance, the fuel levy rates currently
441 implemented in Canada as part of the federal carbon pricing backstop equate to $10 CAD/t
442 $CO_{2(equivalent)}$ for 2018, and are due to increase by $10 CAD/year until a price of $50 CAD/t
443 $CO_{2(equivalent)}$ is reached in 2022 (*91*). Meeting the International Energy Agency (IEA) '2°C
444 Scenario' may result in global marginal abatement costs reaching $130-160 USD/t CO_2 by 2050
445 (*88, 92*), providing incentive for pursuing cost-effective implementation of various mineral
446 carbonation technologies. Additional value could be gained during the implementation of

447 microbial carbonation wetland bioreactors by integrating the biomass component of this carbon
448 sequestration method with biofuel production technologies (*93, 94*).
449

450 **5. Acknowledgements**

451 We acknowledge funding support provided by: Natural Sciences and Engineering Research
452 Council of Canada (NSERC Discovery) (G.S.), Carbon Management Canada (G.M.D. and G.S.),
453 Ontario Graduate Scholarship (J.M.), and NSERC Canada Graduate Scholarship (J.M.). For their
454 technical assistance, we thank Todd Simpson and Tim Goldhawk of the Western Nanofabrication
455 Facility (SEM); Kathryn Green, Richard Webb, Robyn Webb, and Graeme Auchterlonie of the
456 Centre for Microscopy and Microanalysis, The University of Queensland (TEM); and Charles Wu
457 (ICP-AES) and Monique Durr (IC) of the Biotron Institute for Experimental Climate Change
458 Research Analytical Chemistry laboratory. DIC analyses were conducted at The University of
459 British Columbia. Stable isotope analyses were conducted at the G.G. Hatch Stable Isotope
460 Laboratory at The University of Ottawa.
461

462 **Supporting Information**

463 The supplementary information file contains details about the experimental design and the
464 composition of the nutrient and synthetic mine wastewater solutions added to the bioreactor. It
465 reports the errors for the fluid composition measurements and analyses. It also contains additional
466 methods and results for the fluid composition, X-ray diffraction, and electron microscopy analyses,
467 and tables of PHREEQC input data and saturation index outputs.
468

469 **References**

1. Boquet, E.; Boronat, A.; Ramosco, A. Production of calcite (calcium-carbonate) crystals by soil bacteria is a general phenomenon. *Nature* **1973**, *246* (5434), 527-529; 10.1038/246527a0.
2. Merz, M. The biology of carbonate precipitation by cyanobacteria. *Facies* **1992**, *26*, 81-102.
3. Riding, R. Microbial carbonates: the geological record of calcified bacterial-algal mats and biofilms. *Sedimentology* **2000**, *47*, 179-214.
4. Braissant, O.; Decho, A. W.; Dupraz, C.; Glunk, C.; Przekop, K. M.; Visscher, P. T. Exopolymeric substances of sulfate-reducing bacteria: Interactions with calcium at alkaline pH and implication for formation of carbonate minerals. *Geobiology* **2007**, *5*, 401-411; 10.1111/j.1472-4669.2007.00117.x.
5. Gallagher, K.; Kading, T. J.; Braissant, O.; Dupraz, C.; Visscher, P. T. Inside the alkalinity engine: The role of electron donors in the organomineralization potential of sulfate-reducing bacteria. *Geobiology* **2012**, *10*, 518-530; 10.1111/j.1472-4669.2012.00342.x.
6. Ferris, F. G.; Phoenix, V.; Fujita, Y.; Smith, R. W. Kinetics of calcite precipitation induced by ureolytic bacteria at 10 to 20°C in artificial groundwater. *Geochim. Cosmochim. Acta* **2004**, *68* (8), 1701-1710; https://doi.org/10.1016/S0016-7037(03)00503-9.
7. Mitchell, A. C.; Ferris, F. G. The influence of *Bacillus pasteurii* on the nucleation and growth of calcium carbonate. *Geomicrobiol. J.* **2006**, *23* (3-4), 213-226; 10.1080/01490450600724233.
8. Braissant, O.; Cailleau, G.; Aragno, M.; Verrecchia, E. P. Biologically induced mineralization in the tree *Milicia excelsa* (Moraceae): its causes and consequences to the environment. *Geobiology* **2004**, *2* (1), 59-66; 10.1111/j.1472-4677.2004.00019.x.
9. Cailleau, G.; Braissant, O.; Dupraz, C.; Aragno, M.; Verrecchia, E. P. Biologically induced accumulations of $CaCO_3$ in orthox soils of Biga, Ivory Coast. *Catena* **2005**, *59* (1), 1-17; http://dx.doi.org/10.1016/j.catena.2004.06.002.
10. Power, I. M.; Dipple, G. M.; and Southam, G. Bioleaching of ultramafic tailings by *Acidithiobacillus* spp. for CO_2 sequestration. *Environ. Sci. Technol.* **2010**, *44*, 456-462; 10.1021/es900986n.
11. Power, I. M.; Wilson, S. A.; Dipple, G. M.; Southam, G. Modern carbonate microbialites from an asbestos open pit pond, Yukon, Canada. *Geobiology* **2011**, *9*, 180-195; 10.1111/j.1472-4669.2010.00265.x.
12. Power, I. M.; Wilson, S. A.; Small, D. P.; Dipple, G. M.; Wan, W.; Southam, G. Microbially mediated mineral carbonation: Roles of phototrophy and heterotrophy. *Environ. Sci. Technol.* **2011**, *45*, 9061-9068; dx.doi.org/10.1021/es201648g.
13. McCutcheon, J.; Power, I. M.; Harrison, A. L.; Dipple, G. M.; Southam, G. A greenhouse-scale photosynthetic microbial bioreactor for carbon sequestration in magnesium carbonate minerals. *Environ. Sci. Technol.* **2014**, *48* (16), 9142-9151; dx.doi.org/10.1021/es500344s.
14. Harrison, A. L.; Power, I. M.; Dipple, G. M. Accelerated carbonation of brucite in mine tailings for carbon sequestration. *Environ. Sci. Technol.* **2013**, *47* (1), 126-134; dx.doi.org/10.1021/es3012854.
15. Wilson, S. A.; Dipple, G. M.; Power, I. M.; Thom, J. M.; Anderson, R. G.; Raudsepp, M.; Gabite, J. E.; Southam, G. Carbon dioxide fixation within mine wastes of ultramafic-hosted ore deposits: Examples from the Clinton Creek and Cassiar chrysotile deposits, Canada. *Econ. Geol.* **2009**, *104*, 95-112.

16. Washbourne, C. L.; Renforth, P.; Manning, D. A. C. Investigating carbonate formation in urban soils as a method for capture and storage of atmospheric carbon. *Sci. Total Environ.* **2012**, *431*, 166-175; 10.1016/j.scitotenv.2012.05.037.
17. Teir, S.; Eloneva, S.; Zevenhoven, R. Production of precipitated calcium carbonate from calcium silicates and carbon dioxide. *Energy Conversion and Management* **2005**, *46* (18), 2954-2979; https://doi.org/10.1016/j.enconman.2005.02.009.
18. Zhao, H.; Park, Y.; Lee, D. H.; Park, A. H. Tuning the dissolution kinetics of wollastonite via chelating agents for CO_2 sequestration with integrated synthesis of precipitated calcium carbonates. *Phys. Chem. Chem. Phys.* **2013**, *15* (36), 15185-92; 10.1039/c3cp52459k.
19. Huijgen, W. J. J.; Witkamp, G.-J.; Comans, R. N. J. Mechanisms of aqueous wollastonite carbonation as a possible CO_2 sequestration process. *Chem. Eng. Sci.* **2006**, *61* (13), 4242-4251; https://doi.org/10.1016/j.ces.2006.01.048.
20. Gerdemann, S. J.; O'Connor, W. K.; Dahlin, D. C.; Penner, L. R.; Rush, H. Ex situ aqueous mineral carbonation. *Environ. Sci. Technol.* **2007**, *41*, 2587-2593.
21. Park, A.-H. A.; Fan, L.-S. CO_2 mineral sequestration: Physically activated dissolution of serpentine and pH swing process. *Chem. Eng. Sci.* **2004**, *59*, 5241-5247; 10.1016/j.ces.2004.09.008.
22. Park, A. H. A.; Jadhav, R.; Fan, L. S. CO_2 mineral sequestration: Chemically enhanced aqueous carbonation of serpentine. *Can. J. Chem. Eng.* **2003**, *81* (3-4), 885-890.
23. Gadikota, G.; Park, A.-h. A., Chapter 8 - Accelerated carbonation of Ca- and Mg-bearing minerals and industrial wastes using CO_2. In *Carbon Dioxide Utilisation: Closing the Carbon Cycle*, Quadrelli, E. A.; Armstrong, K., Eds. Elsevier: Amsterdam, 2015; pp 115-137.
24. Gadikota, G.; Swanson, E. J.; Zhao, H.; Park, A.-H. A. Experimental design and data analysis for accurate estimation of reaction kinetics and conversion for carbon mineralization. *Ind. Eng. Chem. Res.* **2014**, *53* (16), 6664-6676; 10.1021/ie500393h.
25. Wilson, S. A.; Barker, S. S. L.; Dipple, G. M.; Atudorei, V. Isotopic disequilibrium during uptake of atmospheric CO_2 into mine process waters: Implications for CO_2 sequestration. *Environ. Sci. Technol.* **2010**, *44*, 9522-9529; 10.1021/es1021125.
26. Wilson, S. A.; Raudsepp, M.; Dipple, G. M. Quantifying carbon fixation in trace minerals from processed kimberlite: A comparative study of quantitative methods using X-ray powder diffraction data with applications to the Diavik Diamond Mine, Northwest Territories, Canada. *Appl. Geochem.* **2009**, *24*, 2312-2331; 10.1016/j.apgeochem.2009.09.018.
27. Pronost, J.; Beaudoin, G.; Tremblay, J.; Larachi, F.; Duchesne, J.; Hébert, R.; Constantin, M. Carbon sequestration kinetic and storage capacity of ultramafic mining waste. *Environ. Sci. Technol.* **2011**, *45*, 9413-9420; dx.doi.org/10.1021/es203063a.
28. Beinlich, A.; Austrheim, H. In situ sequestration of atmospheric CO_2 at low temperature and surface cracking of serpentinized peridotite in mine shafts. *Chem. Geol.* **2012**, *332–333*, 32-44; http://dx.doi.org/10.1016/j.chemgeo.2012.09.015.
29. Molson, J. W.; Fala, O.; Aubertin, M.; Bussiere, B. Numerical simulations of pyrite oxidation and acid mine drainage in unsaturated waste rock piles. *J. Contam. Hydrol.* **2005**, *78* (4), 343-371; 10.1016/j.jconhyd.2005.06.005.
30. Mavromatis, V.; Pearce, C. R.; Shirokova, L. S.; Bundeleva, I. A.; Pokrovsky, O. S.; Benezeth, P.; Oelkers, E. H. Magnesium isotope fractionation during hydrous magnesium carbonate precipitation with and without cyanobacteria. *Geochim. Cosmochim. Acta* **2012**, *76*, 161-174; http://dx.doi.org/10.1016/j.gca.2011.10.019.

559 31. Shirokova, L. S.; Mavromatis, V.; Bundeleva, I. A.; Pokrovsky, O. S.; Benezeth, P.;
560 Gerard, E.; Pearce, C. R.; Oelkers, E. H. Using Mg isotopes to trace cyanobacterially mediated
561 magnesium carbonate precipitation in alkaline lakes. *Aquat. Geochem.* **2013**, *19* (1), 1-24;
562 10.1007/s10498-012-9174-3.
563 32. Power, I. M.; Wilson, S. A.; Thom, J. M.; Dipple, G. M.; Southam, G. Biologically induced
564 mineralization of dypingite by cyanobacteria from an alkaline wetland near Atlin, British
565 Columbia, Canada. *Geochem. Trans.* **2007**, *8* (13).
566 33. McCutcheon, J.; Dipple, G. M.; Wilson, S. A.; Southam, G. Production of magnesium-rich
567 solutions by acid leaching of chrysotile: A precursor to field-scale deployment of microbially
568 enabled carbonate mineral precipitation. *Chem. Geol.* **2015**, *413*, 119-131;
569 10.1016/j.chemgeo.2015.08.023.
570 34. Thompson, J. B.; Ferris, F. G. Cyanobacterial precipitation of gypsum, calcite, and
571 magnesite from natural alkaline water. *Geology* **1990**, *18*, 995-998.
572 35. Schultze-Lam, S.; Fortin, D.; Davis, B. S.; Beveridge, T. J. Mineralization of bacterial
573 surfaces. *Chem. Geol.* **1996**, *132* (1-4), 171-181; 10.1016/s0009-2541(96)00053-8.
574 36. Power, I. M.; Wilson, S. A.; Harrison, A. L.; Dipple, G. M.; McCutcheon, J.; Southam, G.;
575 Kenward, P. A. A depositional model for hydromagnesite–magnesite playas near Atlin, British
576 Columbia, Canada. *Sedimentology* **2014**, *61* (6), 1701-1733; 10.1111/sed.12124.
577 37. Power, I. M.; Wilson, S. A.; Thom, J. M.; Dipple, G. M.; Gabites, J. E.; Southam, G. The
578 hydromagnesite playas of Atlin, British Columbia, Canada: A biogeochemical model for CO_2
579 sequestration. *Chem. Geol.* **2009**, *260*, 286-300; 10.1016/j.chemgeo.2009.01.012.
580 38. Power, I. M.; Harrison, A. L.; Dipple, G. M.; Southam, G. Carbon sequestration via
581 carbonic anhydrase facilitated magnesium carbonate precipitation. *Int. J. Greenhouse Gas Control*
582 **2013**, *16*, 145-155; 10.1016/j.ijggc.2013.03.011.
583 39. Peters, K. E.; Walters, C. C.; Moldowan, J. M., *Biomarkers and Isotopes in the*
584 *Environment and Human History*. Cambridge University Press: Cambridge, 2005; Vol. 1, p 1155.
585 40. Vonshak, A., Laboratory techniques for the cultivation of microalgae. In *CRC handbook*
586 *of microalgae mass culture*, Richmond, A., Ed. CRC Press Inc.: Bocca Raton, 1986; p 117.
587 41. McCutcheon, J.; Southam, G. Advanced biofilm staining techniques for TEM and SEM in
588 geomicrobiology: Implications for visualizing EPS architecture, mineral nucleation, and
589 microfossil generation. *Chem. Geol.* **2018**, *498*, 115-127; 10.1016/j.chemgeo.2018.09.016.
590 42. McDonald, K., High-pressure freezing for preservation of high resolution fine structure
591 and antigenicity for immunolabeling. In *Electron Microscopy Methods and Protocols*, Nasser
592 Hajibagheri, M. A., Ed. Humana Press: Totowa, NJ, 1999; Vol. 117, pp 77-97.
593 43. Parkhurst, D. L.; Appelo, C. A. J. *User's guide to PHREEQC (version 2) - A computer*
594 *program for speciation, batch-reaction, one-dimensional transport and inverse geochemical*
595 *calculations*; U.S. Geological Survey: Denver, 1999; pp 99-4259.
596 44. Shuster, J.; Reith, F.; Izawa, M. R. M.; Flemming, R. L.; Banerjee, N. R.; Southam, G.
597 Biogeochemical cycling of silver in acidic, weathering environments. *Minerals* **2017**, *7* (11), 218.
598 45. Mook, W.; Bommerso, J.; Staverma, W. Carbon isotope fractionation between dissolved
599 bicarbonate and gaseous carbon-dioxide. *Earth Planet. Sci. Lett.* **1974**, *22* (2), 169-176;
600 10.1016/0012-821x(74)90078-8.
601 46. Keeling, C. D.; Piper, S. C.; Bacastow, R. B.; Wahlen, M.; Whorf, T. P.; Heimann, M.;
602 Meijer, H. A., *Exchanges of atmospheric CO_2 and $^{13}CO_2$ with the terrestrial biosphere and oceans*
603 *from 1978 to 2000*. Scripps Institution of Oceanography: San Diego, 2001; p 88.

47. Pokrovsky, O. S. Precipitation of calcium and magnesium carbonates from homogeneous supersaturated solutions. *J. Cryst. Growth* **1998**, *186*, 233-239.
48. Spanos, N.; Koutsoukos, P. G. Kinetics of precipitation of calcium carbonate in alkaline pH at constant supersaturation. Spontaneous and seeded growth. *J. Phys. Chem.* **1998**, *102*, 6679-6684.
49. Aizenberg, J.; Black, A. J.; Whitesids, G. M. Control of crystal nucleation by patterned self-assembled monolayers. *Nature* **1999**, *398*, 495-498.
50. Tong, H.; Ma, W.; Wang, L.; Wan, P.; Hu, J.; Cao, L. Control over the crystal phase, shape, size and aggregation of calcium carbonate via a L-aspartic acid inducing process. *Biomaterials* **2004**, *25*, 3923-3929; 10.1016/j.biomaterials.2003.10.038.
51. Power, I. M.; Kenward, P. A.; Dipple, G. M.; Raudsepp, M. Room temperature magnesite precipitation. *Cryst. Growth Des.* **2017**, *17* (11), 5652–5659; 10.1021/acs.cgd.7b00311.
52. Markham, G. D.; Glusker, J. P.; Bock, C. W. The arrangement of first- and second-sphere water molecules in divalent magnesium complexes: Results from molecular orbital and density functional theory and from structural crystallography. *The Journal of Physical Chemistry B* **2002**, *106* (19), 5118-5134; 10.1021/jp020078x.
53. Kluge, S.; Weston, J. Can a hydroxide ligand trigger a change in the coordination number of magnesium ions in biological systems? *Biochemistry* **2005**, *44* (12), 4877-4885; 10.1021/bi047454j.
54. Di Tommaso, D.; de Leeuw, N. H. Structure and dynamics of the hydrated magnesium ion and of the solvated magnesium carbonates: insights from first principles simulations. *Phys. Chem. Chem. Phys.* **2010**, *12* (4), 894-901; 10.1039/b915329b.
55. Slaughter, M.; Hill, R. J. The influence of organic matter in organogenic dolomitization. *J Sediment Petrol* **1991**, *61* (2), 296-303.
56. Wright, D. T.; Wacey, D. Precipitation of dolomite using sulphate-reducing bacteria from the Coorong Region, South Australia: Significance and implications. *Sedimentology* **2005**, *52* (5), 987-1008; 10.1111/j.1365-3091.2005.00732.x.
57. ICDD. International Centre for Diffraction Data. *Magnesite card: 01-071-1534*. **1998**, p 1.
58. Urmos, J.; Sharma, S. K.; Mackenzie, F. T. Characterization of some biogenic carbonates with Raman spectroscopy. *Am. Mineral.* **1991**, *76* (3-4), 641-646.
59. Bischoff, W. D.; Sharma, S. K.; MacKenzie, F. T. Carbonate ion disorder in synthetic and biogenic magnesian calcites; a Raman spectral study. *Am. Mineral.* **1985**, *70* (5-6), 581-589.
60. Wenk, H.-R.; Meisheng, H.; Frisia, S. Partially disordered dolomite; microstructural characterization of Abu Dhabi sabkha carbonates. *Am. Mineral.* **1993**, *78* (7-8), 769-774.
61. Saldi, G. D.; Jordan, G.; Schott, J.; Oelkers, E. H. Magnesite growth rates as a function of temperature and saturation state. *Geochim. Cosmochim. Acta* **2009**, *73*, 5646-5657; 10.1016/j.gca.2009.06.035.
62. Flemming, H.-C.; Wingender, J. The biofilm matrix. *Nat Rev Micro* **2010**, *8* (9), 623-633.
63. Körstgens, V.; Flemming, H.-C.; Wingender, J.; Borchard, W. Influence of calcium ions on the mechanical properties of a model biofilm of mucoid *Pseudomonas aeruginosa*. *Water Science and Technology* **2001**, *43* (6), 49-57.
64. Braissant, O.; Decho, A. W.; Przekop, K. M.; Gallagher, K. L.; Glunk, C.; Dupraz, C.; Visscher, P. T. Characteristics and turnover of exopolymeric substances in a hypersaline microbial mat. *FEMS Microbiol. Ecol.* **2009**, *67* (2), 293-307; 10.1111/j.1574-6941.2008.00614.x.
65. Dupraz, C.; Visscher, P. T. Microbial lithification in marine stromatolites and hypersaline mats. *Trends Microbiol.* **2005**, *13*, 429-438; 10.1016/j.tim.2005.07.008.

66. Altermann, W.; Kazmierczak, J.; Oren, A.; Wright, D. T. Cyanobacterial calcification and its rock-building potential during 3.5 billion years of Earth history. *Geobiology* **2006**, *4*, 147-166.
67. Aloisi, G. The calcium carbonate saturation state in cyanobacterial mats throughout Earth's history. *Geochim. Cosmochim. Acta* **2008**, *72*, 6037-6060; 10.1016/j.gca.2008.10.007.
68. Hänchen, M.; Prigiobbe, V.; Baciocchi, R.; Mazzotti, M. Precipitation in the Mg-carbonate system - effects of temperature and CO_2 pressure. *Chem. Eng. Sci.* **2008**, *63*, 1012-1028; 10.1016/j.ces.2007.09.052.
69. Sánchez-Román, M.; Romanek, C. S.; Fernández-Remolar, D. C.; Sánchez-Navas, A.; McKenzie, J. A.; Pibernat, R. A.; Vasconcelos, C. Aerobic biomineralization of Mg-rich carbonates: Implications for natural environments. *Chem. Geol.* **2011**, *281* (3–4), 143-150; http://dx.doi.org/10.1016/j.chemgeo.2010.11.020.
70. Andres, M. S.; Sumner, D. Y.; Reid, R. P.; Swart, P. K. Isotopic fingerprints of microbial respiration in aragonite from Bahamian stromatolites. *Geology* **2006**, *34* (11), 973-976; 10.1130/g22859a.1.
71. Brady, A. L.; Slater, G. F.; Omelon, C. R.; Southam, G.; Druschel, G.; Andersen, D. T.; Hawes, I.; Laval, B.; Lim, D. S. S. Photosynthetic isotope biosignatures in laminated micro-stromatolitic and non-laminated nodules associated with modern, freshwater microbialites in Pavilion Lake, BC. *Chem. Geol.* **2010**, *274* (1-2), 56-67; 10.1016/j.chemgeo.2010.03.016.
72. Gibson, J. J.; Edwards, T. W. D.; Bursey, G. G.; Prowse, T. D. Estimating evaporation using stable isotopes - Quantitive results and sensitivity analysis for 2 catchments in northern Canadas. *Nord. Hydrol.* **1993**, *24* (2-3), 79-94.
73. Lengke, M.; Southam, G. Bioaccumulation of gold by sulfate-reducing bacteria cultured in the presence of gold(I)-thiosulfate complex. *Geochim. Cosmochim. Acta* **2006**, *70* (14), 3646-3661; http://dx.doi.org/10.1016/j.gca.2006.04.018.
74. Trudinger, P. A.; Chambers, L. A.; Smith, J. W. Low-temperature sulphate reduction: Biological versus abiological. *Can J Earth Sci* **1985**, *22* (12), 1910-1918; 10.1139/e85-207.
75. Revsbech, N. P.; Ward, D. M. Microelectrode studies of interstitial water chemistry and photosynthetic activity in a hot spring microbial mat. *Appl. Environ. Microbiol.* **1984**, *48* (2), 270-5.
76. Jørgensen, B. B.; Revsbech, N. P.; Blackburn, T. H.; Cohen, Y. Diurnal cycle of oxygen and sulfide microgradients and microbial photosynthesis in a cyanobacterial mat sediment. *Appl. Environ. Microbiol.* **1979**, *38* (1), 46-58.
77. Jørgensen, B. B.; Revsbech, N. P.; Cohen, Y. Photosynthesis and structure of benthic microbial mats: Microelectrode and SEM studies of four cyanobacterial communitie. *Limnol. Oceanogr.* **1983**, *28* (6), 1075-1093.
78. Howsley, R. P., H.W. pH dependent sulfide toxicity to oxygenic photosynthesis in cyanobacteria. *FEMS Microbiol Lett* **2006**, *6*, 287-292.
79. Schwermer, C. U.; Lavik, G.; Abed, R. M. M.; Dunsmore, B.; Ferdelman, T. G.; Stoodley, P.; Gieseke, A.; de Beer, D. Impact of nitrate on the structure and function of bacterial biofilm communities in pipelines used for injection of seawater into oil fields. *Appl. Environ. Microbiol.* **2008**, *74* (9), 2841-2851; 10.1128/AEM.02027-07.
80. Joye, S. B.; Paerl, H. W. Nitrogen cycling in microbial mats: Rates and patterns of denitrification and nitrogen fixation. *Mar Biol* **1994**, *119* (2), 285-295; 10.1007/bf00349568.
81. Harrison, A. L.; Dipple, G. M.; Power, I. M.; Mayer, K. U. Influence of surface passivation and water content on mineral reactions in unsaturated porous media: Implications for brucite

695 carbonation and CO_2 sequestration. *Geochim. Cosmochim. Acta* **2015**, *148*, 477-495;
696 http://dx.doi.org/10.1016/j.gca.2014.10.020.
697 82. McCutcheon, J.; Turvey, C. C.; Wilson, S. A.; Hamilton, J. L.; Southam, G. Experimental
698 deployment of microbial mineral carbonation at an asbestos mine: Potential applications to carbon
699 storage and tailings stabilization. *Minerals* **2017**, *7*, 191.
700 83. Hamilton, J. L.; Wilson, S. A.; Morgan, B.; Turvey, C. C.; Paterson, D. J.; MacRae, C.;
701 McCutcheon, J.; Southam, G. Nesquehonite sequesters transition metals and CO_2 during
702 accelerated carbon mineralisation. *Int. J. Greenhouse Gas Control* **2016**, *55*, 73-81;
703 http://dx.doi.org/10.1016/j.ijggc.2016.11.006.
704 84. Hamilton, J. L.; Wilson, S. A.; Morgan, B.; Turvey, C. C.; Paterson, D. J.; Jowitt, S. M.;
705 McCutcheon, J.; Southam, G. Fate of transition metals during passive carbonation of ultramafic
706 mine tailings via air capture with potential for metal resource recovery. *Int. J. Greenhouse Gas*
707 *Control* **2018**, *71*, 155-167; https://doi.org/10.1016/j.ijggc.2018.02.008.
708 85. Wilson, S. A.; Harrison, A. L.; Dipple, G. M.; Power, I. M.; Barker, S. L. L.; Ulrich Mayer,
709 K.; Fallon, S. J.; Raudsepp, M.; Southam, G. Offsetting of CO_2 emissions by air capture in mine
710 tailings at the Mount Keith Nickel Mine, Western Australia: Rates, controls and prospects for
711 carbon neutral mining. *Int. J. Greenhouse Gas Control* **2014**, *25*, 121-140;
712 http://dx.doi.org/10.1016/j.ijggc.2014.04.002.
713 86. Power, I.; McCutcheon, J.; Harrison, A.; Wilson, S.; Dipple, G.; Kelly, S.; Southam, C.;
714 Southam, G. Strategizing carbon-neutral mines: A case for pilot projects. *Minerals* **2014**, *4* (2),
715 399-436.
716 87. Power, I. M.; Harrison, A. L.; Dipple, G. M.; Wilson, S. A.; Kelemen, P. B.; Hitch, M.;
717 Southam, G. Carbon mineralization: From natural analogues to engineered systems. *Rev. Mineral.*
718 *Geochem.* **2013**, *77* (1), 305-360; 10.2138/rmg.2013.77.9.
719 88. High-Level Commission on Carbon Prices *Report of the high-level commission on carbon*
720 *prices*; Washington, DC, 2017; p 69.
721 89. Siegrist, M.; Southam, C.; Bowman, G.; Wilson, S. A.; Southam, G. Analysis of the
722 potential for negative CO_2 emission mine sites through bacteria-mediated carbon mineralisation:
723 Evidence from Australia. *Energy Procedia* **2017**, *114*, 6124-6132;
724 https://doi.org/10.1016/j.egypro.2017.03.1749.
725 90. Siegrist, M.; Southam, C.; Southam, G. In *An economic analysis of the worldwide potential*
726 *for CO_2 sequestration through bacteria-mediated carbon mineralisation at nickel mine sites*, 30th
727 Australasian Finance and Banking Conference 2017, Sydney, Australia, 2017; Sydney, Australia,
728 2017.
729 91. Environment and Climate Change Canada, Technical paper on the federal carbon pricing
730 backstop. In Environment and Climate Change Canada: Gatineau, Canada, 2017; p 22.
731 92. IEA, *Energy Technology Perspectives 2017: Catalysing Energy Technology*
732 *Transformations*. Paris, France, 2017.
733 93. Mata, T. M.; Martins, A. A.; Caetano, N. S. Microalgae for biodiesel production and other
734 applications: A review. *Renewable and Sustainable Energy Reviews* **2010**, *14*, 217–232.
735 94. Ramanan, R.; Kannan, K.; Deshkar, A.; Yadav, R.; Chakrabarti, T. Enhanced algal CO_2
736 sequestration through calcite deposition by *Chlorella* sp. and *Spirulina platensis* in a mini-raceway
737 pond. *Bioresour. Technol.* **2010**, *101*, 2616-2622; 10.1016/j.biortech.2009.10.061.
738

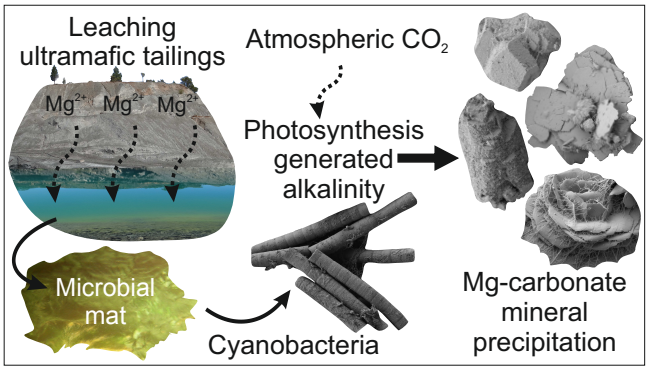
Leaching ultramafic tailings
Mg2+ Mg2+ Mg2+
Atmospheric CO2
Photosynthesis generated alkalinity
Microbial mat
Cyanobacteria
Mg-carbonate mineral precipitation